Structural organization of nuclear lamins A, C, B1, and B2 revealed by superresolution microscopy

Takeshi Shimi[a,*,†], Mark Kittisopikul[b,*], Joseph Tran[c], Anne E. Goldman[a], Stephen A. Adam[a], Yixian Zheng[c], Khuloud Jaqaman[b], and Robert D. Goldman[a]

[a]Department of Cell and Molecular Biology, Northwestern University Feinberg School of Medicine, Chicago, IL 60611; [b]Department of Biophysics, UT Southwestern Medical Center, Dallas, TX 75390; [c]Department of Embryology, Carnegie Institution for Science, Baltimore, MD 21218

ABSTRACT **The nuclear lamina is a key structural element of the metazoan nucleus. However, the structural organization of the major proteins composing the lamina is poorly defined. Using three-dimensional structured illumination microscopy and computational image analysis, we characterized the supramolecular structures of lamin A, C, B1, and B2 in mouse embryo fibroblast nuclei. Each isoform forms a distinct fiber meshwork, with comparable physical characteristics with respect to mesh edge length, mesh face area and shape, and edge connectivity to form faces. Some differences were found in face areas among isoforms due to variation in the edge lengths and number of edges per face, suggesting that each meshwork has somewhat unique assembly characteristics. In fibroblasts null for the expression of either lamins A/C or lamin B1, the remaining lamin meshworks are altered compared with the lamin meshworks in wild-type nuclei or nuclei lacking lamin B2. Nuclei lacking LA/C exhibit slightly enlarged meshwork faces and some shape changes, whereas LB1-deficient nuclei exhibit primarily a substantial increase in face area. These studies demonstrate that individual lamin isoforms assemble into complex networks within the nuclear lamina and that A- and B-type lamins have distinct roles in maintaining the organization of the nuclear lamina.**

Monitoring Editor
Karsten Weis
ETH Zurich

Received: Jul 6, 2015
Revised: Aug 10, 2015
Accepted: Aug 20, 2015

INTRODUCTION

The nuclear lamina is a complex protein network underlying the inner nuclear membrane in metazoan cells. The major structural proteins of the lamina are type V intermediate filament (IF) proteins, the nuclear lamins (Aebi *et al.*, 1986; Fisher *et al.*, 1986; Goldman *et al.*, 1986; McKeon *et al.*, 1986). Lamins are classified as A-type lamins (LA, LC) and B-type lamins (LB1, LB2) based on their sequences and structural properties (Gerace *et al.*, 1978; Gerace and Blobel, 1980). LA and LC are derived from the single *LMNA* gene by alternative splicing (Lin and Worman, 1993). LB1 and LB2 are encoded by two genes, *LMNB1* and *LMNB2* (Hoger *et al.*, 1990; Biamonti *et al.*, 1992; Lin and Worman, 1995; Maeno *et al.*, 1995). In embryonic stem cells, only LB1 and LB2 are abundantly expressed (Constantinescu *et al.*, 2006; Eckersley-Maslin *et al.*, 2013). LB1 continues to be expressed in all cell types throughout development, whereas LA/C and LB2 expression varies across tissues (Stewart and Burke, 1987; Rober *et al.*, 1989). A large number of mutations in the *LMNA* gene causing a wide range of genetic disorders, collectively called laminopathies, often cause misshapen nuclei accompanied by significant changes in chromatin organization (Shimi *et al.*, 2008).

The lamina provides structural support to the nuclear envelope (NE) and is connected to the cytoskeleton through linker of nucleoskeleton to cytoskeleton (LINC) complexes, which span the nuclear membranes (Meinke and Schirmer, 2015). The structural roles of lamins include maintenance of nuclear shape, nuclear positioning, and

This article was published online ahead of print in MBoC in Press (http://www.molbiolcell.org/cgi/doi/10.1091/mbc.E15-07-0461) on August 26, 2015.

*These authors contributed equally and should be regarded as joint first authors.

†Present address: Department of Human Genetics, University of Chicago, Chicago, IL 60637.

Address correspondence to: Robert D. Goldman (r-goldman@northwestern.edu), Khuloud Jaqaman (khuloud.jaqaman@utsouthwestern.edu).

Abbreviations used: IF, intermediate filament; LA, lamin A; LB1, lamin B1; LB2, lamin B2; LC, lamin C; LINC, linker of nucleoskeleton to cytoskeleton; MEFs, mouse embryo fibroblasts; NE, nuclear envelope; NMS, nonmaximal suppression; q-q plot, quantile-quantile plot; 3D-SIM, three-dimensional structured illumination microscopy; wt, wild type.

genome organization. In spite of the important role that lamins play in nuclear structure and function, their organization and structural properties in nuclei have remained elusive. In most somatic cells, the lamina was first described as a thin, electron-dense layer underlying the nuclear membranes, although in some cell types, a thicker structure is apparent (Fawcett, 1966). Electron microscopic images of the native lamina or ectopically expressed lamins in *Xenopus* oocyte nuclei or in nuclei assembled in egg extracts have demonstrated that lamins form meshwork structures at the nucleoplasmic face of the NE (Aebi *et al.*, 1986; Zhang *et al.*, 1996; Goldberg *et al.*, 2008; Grossman *et al.*, 2012). Due to the high density of lamins, chromatin, and other proteins at the nuclear periphery, teasing out details of their structures in somatic cells has proven to be difficult. Three-dimensional structured illumination microscopy (3D-SIM) and confocal microscopy studies have suggested that some lamin isoforms appear to be organized into meshworks in the lamina of mouse and human cell nuclei (Schermelleh *et al.*, 2008; Shimi *et al.*, 2008).

Cytoplasmic IFs form 10-nm fibers organized into complex networks with important roles in regulating the mechanical properties of the cytoplasm (Guo *et al.*, 2013). Similar to all cytoskeletal IF proteins, lamins have an α-helical central rod domain flanked by short, globular N-terminal "head" and long C-terminal "tail" domains (Parry *et al.*, 1986). In vitro, lamins form coiled-coil dimers through interactions of their central rod domains, which further associate end to end to form polar head-to-tail protofilaments (Heitlinger *et al.*, 1991; Stuurman *et al.*, 1996). These head-to-tail protofilaments associate laterally in a half-staggered, antiparallel manner to form apolar tetrameric filaments that ultimately interact to form paracrystalline arrays (Heitlinger *et al.*, 1991; Stuurman *et al.*, 1996; Ben-Harush *et al.*, 2009). In spite of the relatively detailed information on lamin structure in vitro, little is known about their native supramolecular structures in the lamina in intact cells.

Lamins and their associated proteins organize chromatin into functional domains called lamina-associated domains (LADs) at the nuclear periphery (Guelen *et al.*, 2008; Zullo *et al.*, 2012). Whereas numerous studies have indicated that LA and LB1 interact largely with the same regions of chromatin, other studies have suggested that the distribution of lamin–chromatin interactions is more complex (Zullo *et al.*, 2012; Eckersley-Maslin *et al.*, 2013; Meuleman *et al.*, 2013; Lund *et al.*, 2014, 2015; Harr *et al.*, 2015; Zheng *et al.*, 2015). To begin to understand the functions of the lamins, especially with respect to their roles in chromatin organization and gene expression, it is important to determine the types of supramolecular structures they form in the nuclear lamina of somatic cells. A major unresolved issue concerning lamina supramolecular structure is how the four lamin isoforms are organized and whether or not each of the isoforms exists as a distinct polymer network. Previously, we demonstrated by confocal microscopy that A- and B-type lamins formed separate but interacting meshworks of fibrils within the lamina of HeLa cell nuclei (Shimi *et al.*, 2008). Another study by deconvolution microscopy demonstrated that LA and LC were localized in partially distinct regions within the lamina (Kolb *et al.*, 2011). If each of the lamin isoforms is organized into a distinct network in the lamina, it is also important to know whether these networks interact with or influence each other. To begin to address these questions and provide a more complete picture of lamin organization and structure in normal cells, we carried out a detailed examination of each lamin isoform using 3D-SIM, computational image analysis, and quantitative meshwork characterization.

RESULTS

Lamin isoforms are organized into distinct supramolecular structures in the nuclear lamina

To determine the structural relationship of each lamin isoform to the others in a single cell type, we colocalized pairs of all four lamin isoforms in immortalized mouse embryo fibroblasts (MEFs) by immunofluorescence with specific antibodies to each isoform. Because the lamins are densely packed in the lamina, achieving adequate resolution of the different isoforms required the use of 3D-SIM (see *Materials and Methods*). Imaging the entire lamina at the resolution achievable with 3D-SIM was challenging due to the high degree of curvature of the nuclear surface in most cultured cells. However, the relatively flat nuclei of MEFs compared with nuclei of other cell types allowed us to focus on large areas of the lamina. Our reconstructed 3D-SIM images of double-labeled nuclei showed that in all staining combinations, each lamin isoform appeared to be mostly distinct from the other lamin isoforms (Figure 1). However, in some areas of the lamina, a small amount of overlap between lamin isoforms could be seen.

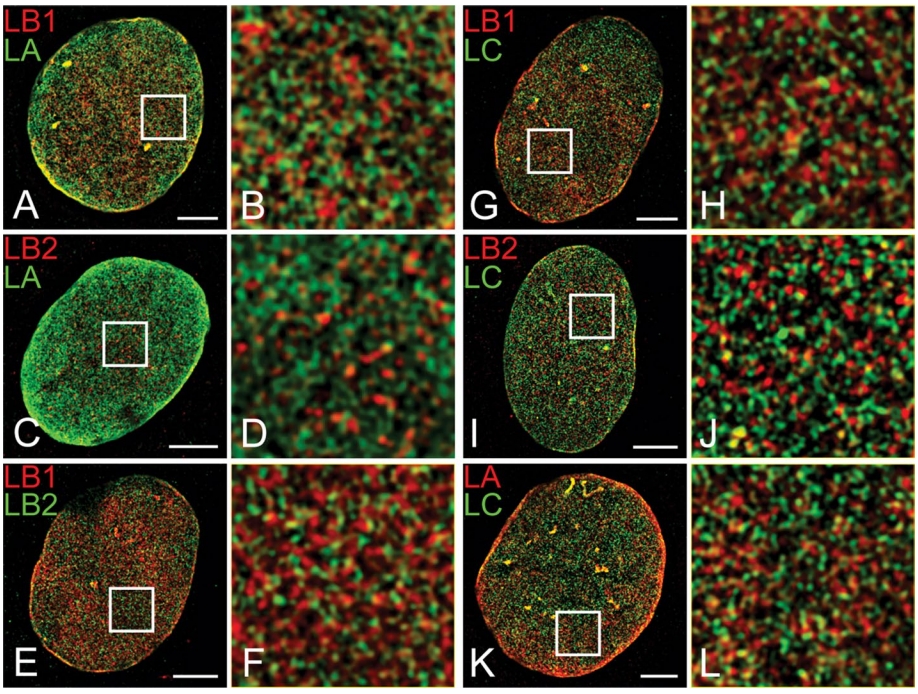

FIGURE 1: Colocalization of lamin isoforms in MEFs using indirect immunofluorescence and 3D-SIM. Specific antibodies for pairs of lamin isoforms in all combinations. (A, B) LB1/LA, (C, D) LB2/LA, (E, F) LB1/LB2, (G, H) LB1/LC, (I, J) LB2/LC, and (K, L) LA/LC. The areas indicated by white squares in A, C, E, G, I, and K are magnified approximately fivefold along each edge in B, D, F, H, J, and L, respectively. Scale bar, 5 μm.

The patterns of LA and LB1 in the lamina appeared as networks of short, fibrous structures with some discontinuous patches (Figure 1, B, D, F, H, and L). On the other hand, LB2 and LC appeared predominantly as discrete spots or islands of short fibers (Figure 1, D, F, H, and J, and Supplemental Figure S1), although the spots often had a "beads-on-a-string" appearance

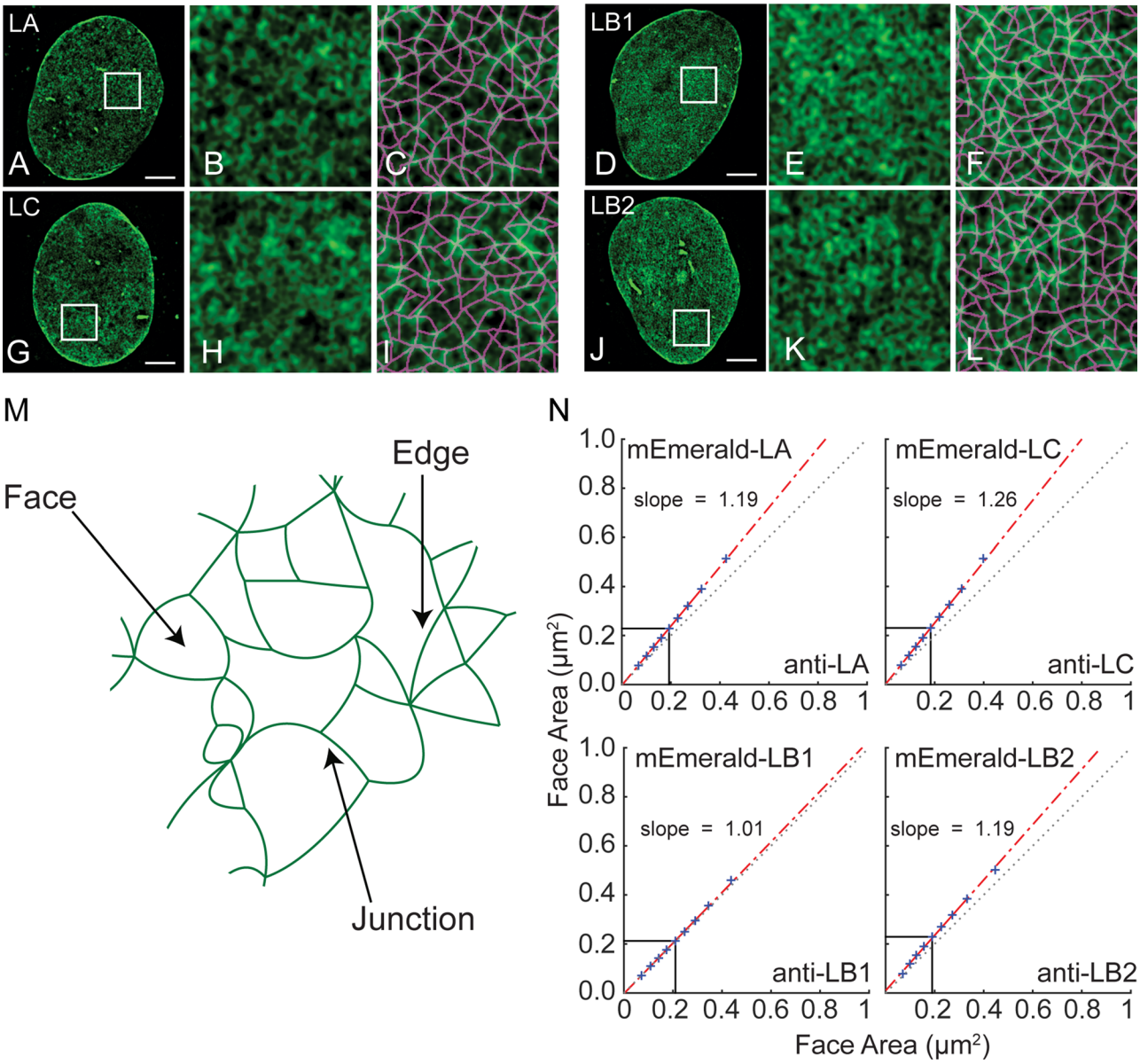

FIGURE 2: mEmerald-lamin isoforms localized by 3D-SIM. mEmerald-tagged lamins were transiently expressed in immortalized MEFs, followed by fixation. (A) Emerald-LA, (D) Emerald-LB1, (G) Emerald-LC, and (J) Emerald-LB2. The areas indicated by white squares are enlarged approximately fivefold along each edge in B, E, H, and K. Detected meshworks from automated computer image analysis (C, F, I, L) are overlaid in magenta on the respective magnified region. (M) A lamin meshwork is illustrated depicting a junction, an edge, and a face. (N) Distributions of the areas of faces in square micrometers of the Emerald-lamin fusions on the *y*-axis vs. the corresponding distribution of face areas from the immunofluorescence on the *x*-axis in q-q plots. The blue x's indicate the 10th through 90th matched percentiles in decade intervals. The 50th percentile, or median, is indicated by black lines. The red line is a linear regression from the 25th to the 75th percentile with slope as indicated. A dotted gray line indicates a line with slope of 1 and an intercept of 0. Scale bar, 5 μm.

(Supplemental Figure S1, arrows). This spotty staining pattern could be due to either antibody accessibility or an inability of LC and LB2 to form connected networks in MEFs. To differentiate between these possibilities, we expressed mEmerald-tagged lamins in MEFs and imaged the resulting supramolecular structures by 3D-SIM. The images of fixed cells showed that all mEmerald-lamins formed apparently continuous networks in the lamina, with linear structures clearly visible (Figure 2, B, E, H, and K). This result supports the likelihood that the spotty staining patterns of LB2 and LC obtained by immunofluorescence were due to issues with antibody accessibility.

The lamins form similar meshwork structures in the lamina

The high density of lamins in the 3D-SIM images made it difficult to visually discern details of their overall structures. To obtain quantitative information on the properties of the lamin networks observed by antibody localization and mEmerald-tagged lamins, we subjected the reconstructed 3D-SIM images to computational image analysis. To minimize artifacts from nuclear envelope curvature, we focused our analysis on the bottom surface of the nucleus, which was flat and parallel to the coverslip. Before segmentation, the *z*-slice containing the bottom surface of the nucleus was processed

using a steerable line filter to enhance line signals in the image (Freeman and Adelson, 1991; Jacob and Unser, 2004). The steerable filter response was then thresholded, and the centers of the lines—derived via nonmaximal signal suppression (Canny, 1986)—were taken as the most likely positions of the meshwork edges, that is, the lamin fibers making the meshwork (Figure 2M). These operations yielded almost the full meshwork, at the expense of generating gaps in the edges at junctions (intersections of two or more edges; Figure 2M). To close these gaps, which were usually two to three pixels, we extended the detected lines each along its direction until it encountered another line, thus identifying junctions (Figure 2M). To ensure that there was no oversegmentation, we then audited the resulting meshwork edges and retained only those above the quality threshold—derived from intensity levels and variations—yielding the final meshwork (Figure 2, C, F, I, and L, and Supplemental Figure S2; see *Materials and Methods* for more details). In the final meshwork, faces were defined as areas surrounded by edges that are themselves devoid of lamins (Figure 2M). Of note, each edge is the result of a curvilinear lamin signal from junction to junction, without any knowledge of its higher-resolution structural makeup, as this information is not accessible via SIM. Although only meshworks over small areas are shown in the figures for visual clarity, the quantitative meshwork analyses discussed later were performed on entire images of the lamina region of the bottom surface of the nucleus (Supplemental Table S1 lists number of cells and number of faces analyzed for all conditions presented in this study).

First we compared the mEmerald-lamin meshworks to those obtained by immunofluorescence labeling of the endogenous protein to investigate whether the two labeling approaches revealed similar meshworks. Although LB2 and LC images appeared somewhat punctate by immunofluorescence, we reasoned that our line filtering and meshwork segmentation might be able to connect the dots and reveal the underlying meshwork for these two lamins, especially with their "beads-on-a-string" appearance. To validate this approach, we compared the face area between the two labeling modalities using quantile-quantile plots (q-q plots; Figure 2N), which permitted comparison of the full distribution of values instead of only one value such as the mean or median. The q-q plots also allowed us to detect differences between two distributions even if they were only at one end or the other, without global shifts in the whole distribution. This analysis revealed that the mEmerald-LB1 and immunofluorescence images of the LB1 meshworks were almost identical, whereas the mEmerald-lamin and immunofluorescence image meshworks of LA, LB2, and LC were very similar but with slightly larger faces in the mEmerald cases (slope > 1; slopes farther from 1 indicate larger differences). These results increased our confidence in defining the structural properties of the meshworks detected by immunofluorescence, especially in the case of LB2 and LC.

Next we compared the meshwork properties between the different lamins from the two-color immunofluorescence images (Figure 1). The face-area q-q plots (Figure 3, A–F) comparing the different lamins showed that overall they were quite similar, although with some clear differences. Specifically, LB1 exhibited larger faces than the other lamins (Figure 3, A, C, and D), and LA in turn exhibited larger faces than LC (Figure 3F). These differences in face area could be due to differences in edge length (Figure 3, G–L, and Table 1), edge connectivity (Figure 3, M–R, and Table 1), face shape (measured as circularity; Table 1), or a combination of these properties. We found that LB1 had a larger proportion of faces with greater mean edge length than LA and LC but not LB2 (Figure 3, G, I, and J). However, LB1 tended to have more edges per face (a measure of edge connectivity) than LB2 (Figure 3O). Similarly, LA meshworks exhibited more edges per face than LC meshworks (Figure 3R).

Because relative increases in mean edge length and edges per face seemed to account for the increases in face area, we developed a formula that would approximately relate these factors to each other. Given that face perimeter = mean edge length × number of edges per face, we expected the corresponding linear scaling factors (m) to approximately share the same relation:

$$m_{\text{perimeter}} \approx m_{\text{edges per face}} \times m_{\text{mean edge length per face}} \quad (1)$$

Furthermore, circularity is a measure of shape that relates the face perimeter to the face area. Thus we can also relate their corresponding scaling factors:

$$\text{circularity} \equiv \frac{4\pi\,\text{area}}{\text{perimeter}^2} \quad (2)$$

$$m_{\text{area}} \approx m_{\text{circularity}} \times m^2_{\text{perimeter}} \quad (3)$$

Indeed, we see that for all of our data, the product relation (Eq. 1) held to yield the perimeter scaling factor, and the square of the perimeter scaling factor was closely related to the area scaling as in Eq. 3 (Table 1). Furthermore, the circularity scaling factors were near 1, meaning that the overall distributions of face shapes were not changing. Instead, the faces were altered primarily because of changes in edge length or edge connectivity, measured as number of edges per face. Of note, the differences in edge length and number of edges per face seemed to vary in an uncoupled manner among lamin isoforms, suggesting that these two properties are relatively independent characteristics of the meshworks. Our present analyses suggest that we can relate most of the variations in meshwork property distributions through linear scaling factors.

Structural alterations of lamin meshworks in *Lmna*$^{-/-}$ and *Lmnb1*$^{-/-}$ MEFs

Our previous studies found that decreasing the amount of LB1 in cells by short hairpin RNA–mediated silencing led to an enlarging of the A-type lamin meshwork structure in HeLa cells, suggesting that the A- and B-type lamin meshworks interact in some way (Shimi *et al.*, 2008). To obtain a quantitative measure of possible lamin meshwork changes when one lamin isoform is absent, we analyzed and compared meshwork structures in MEFs derived from wild-type (wt) and *Lmna*, *Lmnb1*, and *Lmnb2* knockout mice (Kim *et al.*, 2011, 2013; Guo *et al.*, 2014) by 3D-SIM (Figure 4). For these experiments, we used monoclonal antibodies that recognize both LA and LC or LB1 and LB2.

Approximately 106 of 226 nuclei of *Lmnb1*$^{-/-}$ MEFs imaged by 3D-SIM showed qualitative enlargement of the LA/C meshwork faces (Figure 4, D–F). This enlargement was supported by quantitative analysis of a representative sampling of *Lmnb1*$^{-/-}$MEFs with enlarged meshwork faces (Supplemental Table S1C). We found a quantitative increase in face area over wt of 34% in terms of the overall distribution, along with an increase of face areas in the top 5th percentile (Figure 4N and Table 1C). This increase in face area appears to be due to a 10% increase in the number of edges per face and a 7% increase in the mean edge length per face (Figure 4, Q and T, and Table 1). Similar to *Lmnb1*$^{-/-}$MEFs, 130 of 224 nuclei imaged in *Lmna*$^{-/-}$ MEFs, showed qualitative enlargement of the LB1/2 meshwork faces (Figure 4, G–I). Quantitatively, face areas in *Lmna*$^{-/-}$ nuclei increased by 20% in scale over wt when comparing the distributions of wt and null nuclei in a representative sample

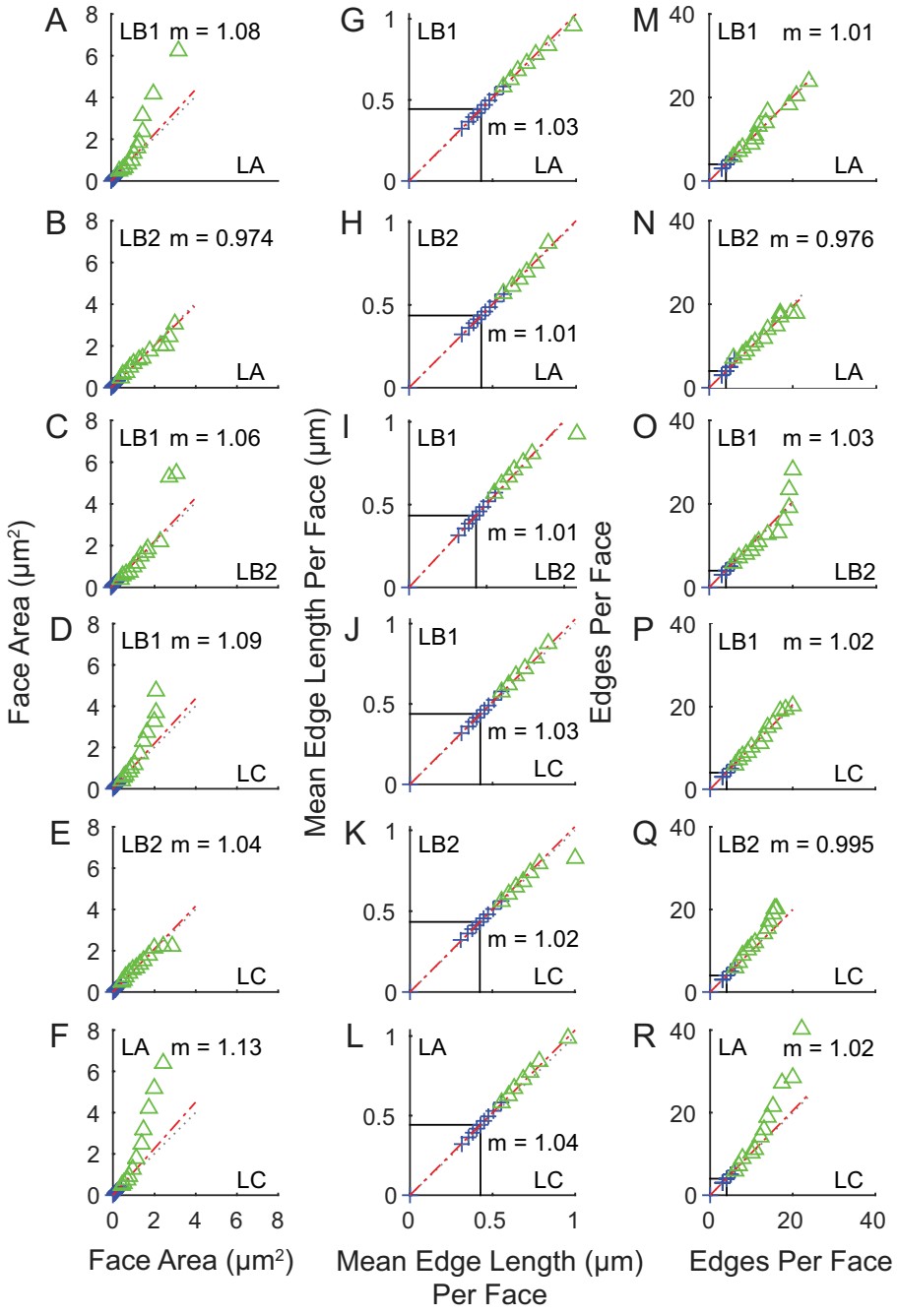

FIGURE 3: Quantile-quantile plots comparing the distribution of meshwork parameters for all lamin isoforms detected by two-color immunofluorescence. (A–F) face areas of the lamin meshworks, (G–L) mean edge length per face, and (M–R) number of edges per face. The 50th percentile, or median, is indicated by black lines. A dotted gray line indicates a line with slope of 1 and an intercept of 0. The red line is a linear regression from the 25th to the 75 percentile with slope as indicated. The slope of the red line, *m*, is indicated. The blue crosses indicate the 10th–90th matched percentiles in decade intervals. Green triangles represent the 95th, 97.5th, 98.75th, 99.38th, 99.96th, 99.99th, and 100th matched percentiles to illustrate the behavior of the upper tail of the distribution.

(Supplemental Table S1C and Figure 4M). This increase in face area is distinct from that observed in *Lmnb1*$^{-/-}$, as an increase in mean edge length (6%) contributed more than an increase in meshwork complexity (3%) measured as edges per face (Figure 4, P and S, and Table 1). In contrast, the face areas in *Lmnb2*$^{-/-}$ MEFs were qualitatively similar to those in wt nuclei (Figure 4, A–C and J–L). Quantitatively, we observed an 8% increase in face area scaling (Figure 4O and Supplemental Table S1C), which was predicted by a corresponding 3% increase in mean edge length per face (Figure 4R and Table 1) and a 1% increase in edges per face (Figure 4U and Table 1) when comparing distributions. In summary, whereas all the meshworks observed from knockouts exhibited enlarged face areas, *Lmnb1*$^{-/-}$ meshworks had the most dramatic change, with corresponding changes in both mean edge length and number of edges compared with the others. *Lmna*$^{-/-}$ meshworks showed a more moderate increase in face area versus wild type, and this appears to be achieved mainly by increasing mean edge length per face scale, whereas *Lmnb2*$^{-/-}$ meshworks showed the smallest increase in scale for all properties compared with the others versus wild type, with most of the change originating from increased mean edge length per face.

Because changes in face perimeter and related properties (Table 1C) could largely explain the increases in face area, this suggested that the shape of faces in the lamin-knockout nuclei were overall similar compared with wild type. Indeed, in examining circularity as a measure of shape, we saw that the distributions of shapes were unchanged, with all of the scaling factors near 1 (Table 1C). However, circularity can be inaccurate due to the discretization of space for faces of small area. Eccentricity is another measure of face shape and more robustly measures how much a face deviates from a circle as it becomes more oblong. Whereas the overall scaling factors were consistent with the circularity analysis (Figure 4, V–X), the eccentricity measure revealed differences in the lower tail of the distributions. Specifically, whereas wt LB1/2 meshworks contained a subset of faces with an almost circular shape (eccentricity near 0), the *Lmna*$^{-/-}$ MEFs exhibited a smaller proportion of faces with an eccentricity value of <0.2 (Figure 4, G–I and V).

Overall, structural alterations of lamin meshworks in the knockout MEFs appear to be mainly effected by changes in the perimeter of faces through either the mean edge length or the number of edges per face. Which property is affected and to what degree depend on the lamin subtype removed. *Lmna*$^{-/-}$ primarily alters mean edge length per face, whereas *Lmnb1*$^{-/-}$ affects both properties. *Lmna*$^{-/-}$ also changes the tail of the eccentricity such that faces are less likely to be circular. The relatively small change in *Lmnb2*$^{-/-}$ is mediated mainly by a change in mean edge length per face. Because the shape distribution of the faces is mostly unchanged, these changes in face perimeter in turn translate into corresponding changes in face area (Table 1C and Eq. 3).

Query	Reference	Face area	Edges per face	Mean edge length per face	Perimeter	Perimeter^2	Circularity	Perimeter^2 × circularity
A. Wild-type mEmerald vs. immunofluorescence								
mEmerald-LA	α-LA	1.187	1.025	1.061	1.093	1.194	0.996	1.190
mEmerald-LB1	α-LB1	1.012	1.000	1.004	1.007	1.013	0.997	1.011
mEmerald-LB2	α-LB2	1.190	1.036	1.054	1.097	1.203	0.994	1.197
mEmerald-LC	α-LC	1.258	1.038	1.082	1.127	1.269	0.992	1.259
B. Wild-type lamin subtypes in the same cells								
α-LB1	α-LA	1.083	1.008	1.030	1.042	1.085	1.001	1.086
α-LB2	α-LA	0.974	0.976	1.008	0.989	0.977	0.994	0.972
α-LB1	α-LB2	1.056	1.027	1.008	1.034	1.069	0.996	1.065
α-LB1	α-LC	1.091	1.025	1.028	1.052	1.107	0.989	1.095
α-LB2	α-LC	1.039	0.995	1.021	1.021	1.042	0.996	1.038
α-LA	α-LC	1.125	1.024	1.038	1.063	1.130	0.997	1.127
C. Lamin knockouts vs. wild type								
Lmna$^{-/-}$ α-LB1/2	wt α-LB1/2	1.202	1.027	1.059	1.094	1.198	1.001	1.199
Lmnb1$^{-/-}$ α-LA/C	wt α-LA/C	1.341	1.095	1.067	1.169	1.366	0.986	1.346
Lmnb2$^{-/-}$ α-LA/C	wt α-LA/C	1.077	1.008	1.029	1.037	1.076	0.997	1.073

The slope of a linear regression through the 25th through the 75th percentile in q-q plots represents a linear scaling factor that relates the query distribution to the reference. The scaling factor is shown for the following meshwork properties: face area, edges per face, mean edge length per face, face perimeter, and face circularity. In addition, the square of the face perimeter scaling factor and its product with the face circularity scaling factor are shown for comparison with the area scaling factor. All scaling factors are unitless. Underlined values indicate that the query and reference distributions are not significantly different by the Mann–Whitney *U* test at the 0.05 significance level with Bonferroni correction applied for 91 comparisons. (A) Meshwork properties from mEmerald are compared with properties from immunofluorescence. (B) Meshwork properties from lamin subtypes are compared against each other from the same set of cells. (C) Meshwork properties from lamin knockouts are compared against wild type using the same immunofluorescence label.

TABLE 1: Quantile-quantile scaling factors.

The overall similarities and differences between the meshworks under the different conditions can be visually summarized as a scatter plot of mean edge length per face versus number of edges per face (Figure 5). Such a depiction is possible because 1) these two properties were the two most-varying properties between the different lamin isoforms and between wt and knockout MEFs, and 2) these two properties appear to vary independently of each other, and together they account for most of the observed variations in face area. For this scatter plot, we took native LA in wt cells as a reference, with mean edge length per face of 0.432 μm (median value) and number of edges per face of four (median value). Using these reference values and the q-q plot scaling factors (Table 1), we then positioned all other lamins and conditions on the scatter plot. This strategy enabled us to overcome the discretization issues that confounded the detection of variations between the different lamins and conditions by direct calculation of their median number of edges per face. This scatter plot readily reveals the large effect that the knockout of LA or LB1 has on the remaining meshworks (Figure 5, blue x's) and the more subtle differences between the different lamins in wt cells (red circles) and between immunolabeled and overexpressed lamins (green squares). It also reveals the contribution of each of the two properties toward the observed variations.

DISCUSSION

Using 3D-SIM and computational image analysis, we demonstrate that lamins A, C, B1, and B2 are each present as distinct meshworks within the lamina of MEF nuclei. Using a steerable line filter to process the 3D-SIM images, we performed segmentation analyses to reconstruct the lamin meshworks from complex images. These reconstructions provided quantitative information on edge length, face area, and edge connectivity forming the meshworks. The results demonstrate that the meshworks are remarkably similar in physical characteristics, with only small differences in the face sizes of each lamin isoform. We validated the segmentation of meshworks by comparing the endogenous lamin structures labeled with antibodies to the structures obtained by the ectopic expression of mEmerald-tagged lamins. The two methods yielded almost identical results for LB1 and very similar results for LB2, LA, and LC. In this regard, the sensitivity of the automated segmentation based on line filters was critical for revealing structure in images that by eye had no obvious meshworks, such as for antibody labeling of the LB2 and LC meshworks.

The distinct meshworks of the lamin isoforms in the lamina do not preclude interactions between the lamin meshworks. In fact, our findings of lamin meshwork changes in *Lmna*$^{-/-}$ and *Lmnb1*$^{-/-}$ null MEFs demonstrate that the meshwork properties of individual lamins depend on the presence of the other lamins. Cells lacking either LA/C or LB1 showed large alterations in the structure of the remaining meshworks, but the lack of LB2 had only minor effects on the remaining lamins. Our previous studies showed that the total lamin amount is critical for the formation of a dense lamin meshwork (Guo *et al.*, 2014). The relatively minor effects of LB2 deletion on the remaining lamin meshworks could be due to a lower concentration of LB2 relative to the other isoforms or to compensation by the remaining lamin meshworks. Alternatively, it is possible that LB2 is simply not required for the proper structure of the other lamin meshworks. It is also not clear why only approximately half of the cells lacking LA/C or LB1 show alterations in meshwork structure. The possibilities

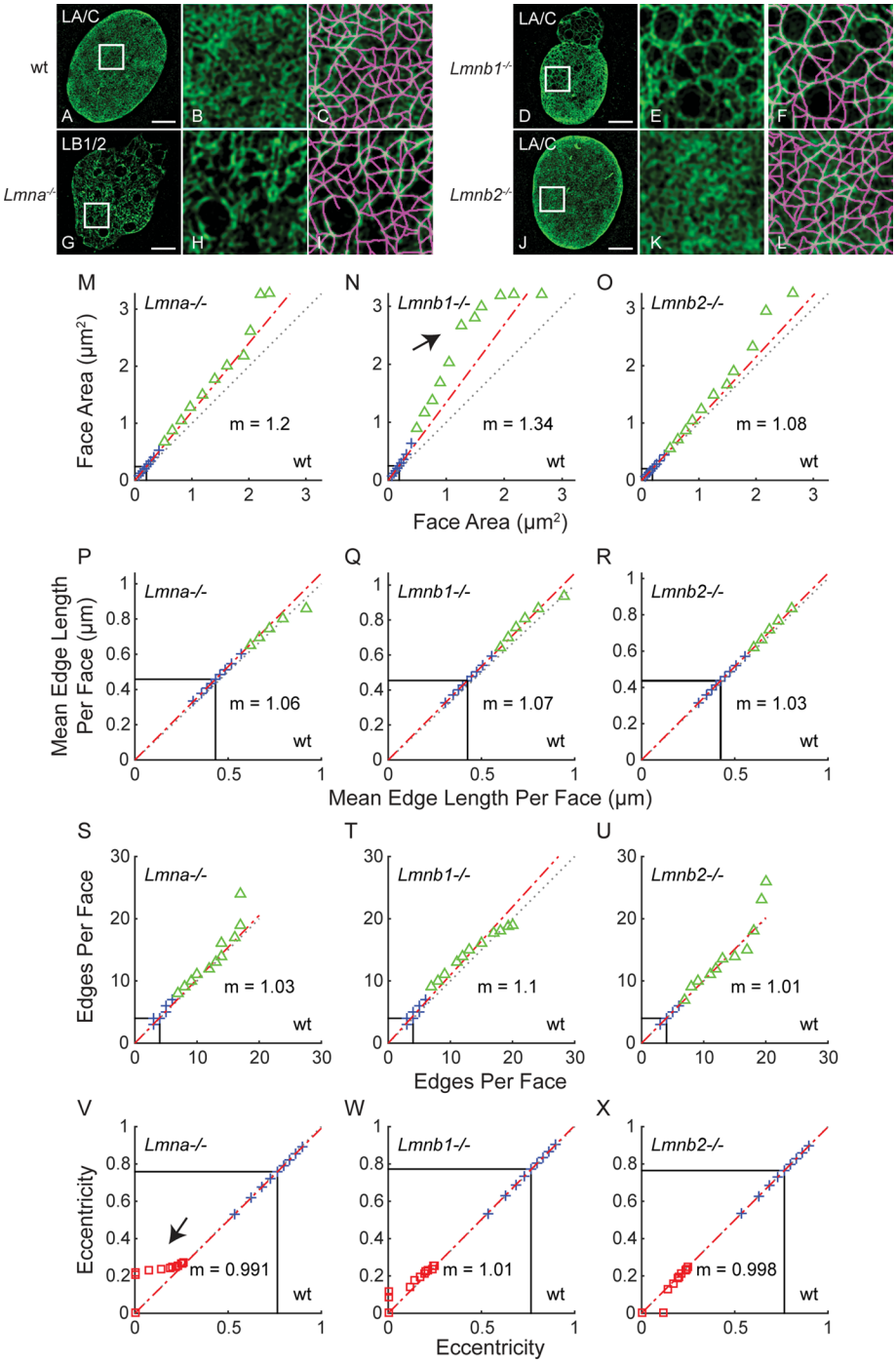

FIGURE 4: Quantitative analyses of lamin meshworks in lamin-null MEFs. Examples of 3D-SIM images of lamin meshworks and automated image analysis from (A–C) wt, (D–F) *Lmnb1*$^{-/-}$, (G–I) *Lmna*$^{-/-}$, and (J–L) *Lmnb*$^{-/-}$MEFs. LA/C in wt, *Lmnb1*$^{-/-}$, and *Lmnb2*$^{-/-}$MEFs and LB1/2 in *Lmna*$^{-/-}$ MEFs were localized by immunofluorescence. Areas indicated by white squares in B, E, H, and K are enlarged approximately fivefold along each edge in C, F, I, and L, respectively, and meshworks detected by automated image analysis are shown in magenta to the right of the magnified images. Scale bar, 5 μm. *Lmna*$^{-/-}$, *Lmnb1*$^{-/-}$, and *Lmnb2*$^{-/-}$ MEFs were compared with wt MEFs with regard to (M–O) face area, (P–R) mean edge length per face, (S–U) edges per face, and (V–X) face eccentricity distributions using q-q plots. The 50th percentile, or median, is indicated by black lines. The red line is a linear regression from the 25th to the 75th percentile with slope as indicated. A dotted gray line indicates a line with a slope of 1 and an intercept of 0. The blue x's indicate the 10th through 90th matched percentiles in decade intervals. Green triangles represent the 95th, 97.5th, 98.75th, 99.38th, 99.96th, 99.99th, and 100th matched percentiles to illustrate the behavior of the upper tail of the distribution. Red squares indicate the 0th, 0.63th, 0.66th, 0.69th, 0.72th, 0.76th, 0.79th, 0.83th, 0.87th, 0.91th, and 0.96th percentiles to illustrate the lower 1st percentile tail of the eccentricity distribution. Black arrows indicate positive deviations from the red line, indicating a right shift in the (N) face area for *Lmnb1*$^{-/-}$ MEFs and (V) eccentricity distributions for *Lmna*$^{-/-}$ MEFs.

include, but are not limited to, cell cycle differences, compensating protein expression, or the presence of different types of fibroblasts in the MEF population. Previous studies support the idea that the lamin meshworks interact and influence each other's behavior and structure. Partial silencing of lamin expression in cultured cells and gene knockouts in mice also lead to the formation of abnormally shaped nuclei and the formation of enlarged lamin meshwork structures (Sullivan *et al.*, 1999; Vergnes *et al.*, 2004; Shimi *et al.*, 2008; Guo *et al.*, 2014). Laminopathy mutations in *LMNA* have also been shown to lead to the formation of enlarged lamin meshworks (Vigouroux *et al.*, 2001; Novelli *et al.*, 2002; Muchir *et al.*, 2004). These findings all support a model for lamina structure in which the individual lamin isoforms interact in some way and influence each other's structures. Identifying the factors responsible for assembling and maintaining lamin meshworks should be aided by our quantitative methods for analyzing lamin supramolecular structures.

In future studies, it will also be important to determine how the different lamin isoforms assemble into mainly distinct yet connected structures. Clues may be derived from studies of lamin assembly after mitosis. During mitotic prophase, the lamina and the rest of the NE disassemble, and their components are dispersed throughout the cell. Disassembly of the lamins is coupled to their phosphorylation at specific residues maintaining them in a nonpolymerized form (Moir *et al.*, 2000). LB1 and LB2 remain associated with the nuclear membranes absorbed into the ER due to their farnesyl anchors, whereas LA and LC disperse into the cytoplasm. Studies of the reassembly of the lamina beginning in telophase suggest that the lamin isoform meshworks may assemble as separate structures. For example, in HeLa cells, some LA/C begins to accumulate at the "core" regions of chromosomes in close association with kinetochores during early telophase (Dechat *et al.*, 2007; Haraguchi *et al.*, 2008). In HeLa and other cells, the bulk of LA/C is only assembled at late telophase and early G1 after transport across the reformed NE is established (Moir *et al.*, 2000; Dechat *et al.*, 2007; Haraguchi *et al.*, 2008). In contrast, LB1 and LB2 accumulate

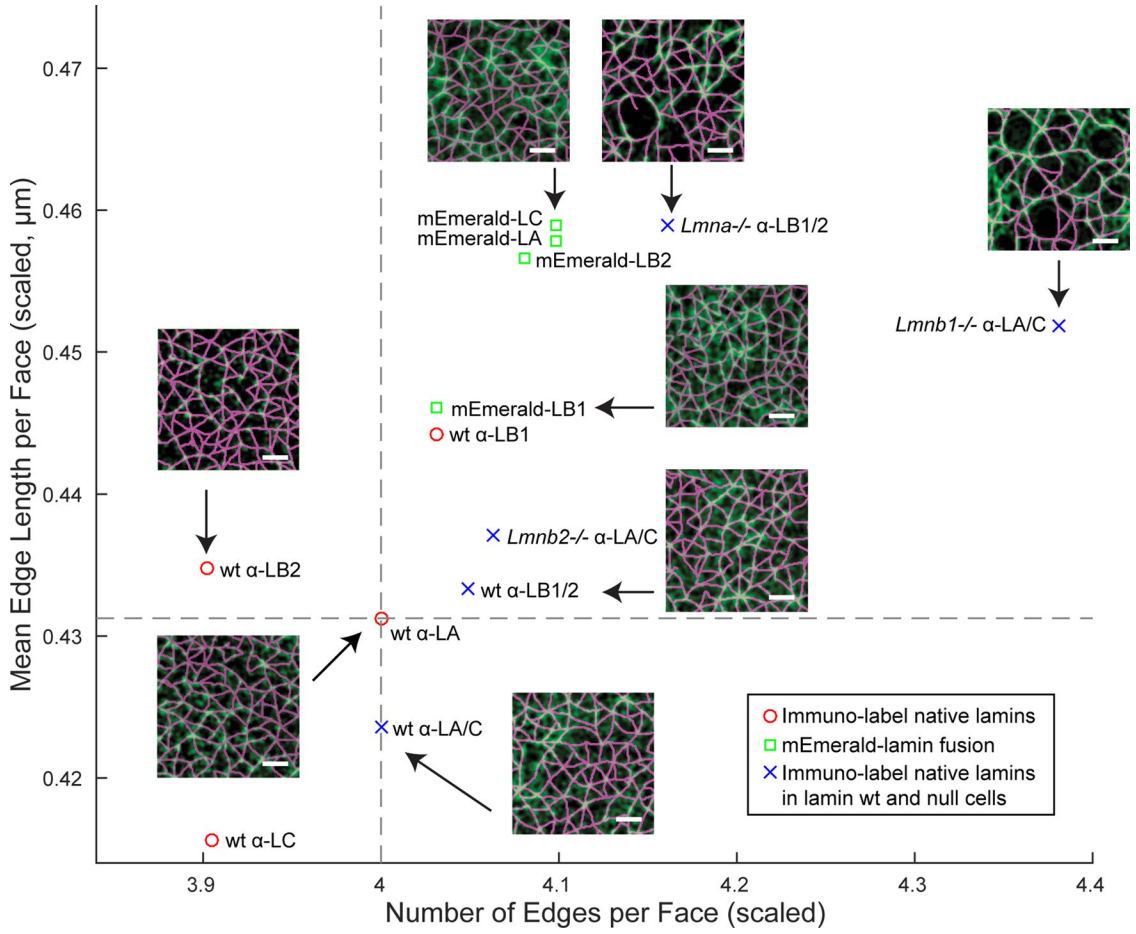

FIGURE 5: Summary of results. The mean edge length per face is plotted against the number of edges per face. The values are scaled according to the scaling factors in Table 1, which were computed from a linear regression of the 25th to the 75th percentiles for each distribution. The median values for LA were used as a reference as indicated by the gray dashed lines. Example images are included and correspond to points indicated by the black arrows. Red circles indicate data from indirect immunofluorescence of MEFs in Figure 1 and Supplemental Figure S1. Green squares indicate mEmerald-lamin isoforms in Figure 2. Blue x's indicate indirect immunofluorescence of MEFs and lamin-null MEFs in Figure 4. Scale bars, 1 µm.

around daughter chromosomes with the nuclear membranes at late telophase in HeLa cells (Haraguchi *et al.*, 2008). These B-type lamins are excluded from core regions and are incorporated into the re-forming lamina/NE much earlier than LA and LC (Moir *et al.*, 2000). Less is known about the assembly of lamins during interphase. In early G1 phase, HeLa S3 cells contain regions of the NE devoid of NPCs called "pore-free islands" (Maeshima *et al.*, 2006; Haraguchi *et al.*, 2008). These areas are enriched in LA and LC but devoid of LB1 and LB2 (Maeshima *et al.*, 2006). These findings all support the idea that the lamin isoforms assemble into separate meshwork structures, and this separation may be driven by their different mechanisms of assembly after mitosis.

Although superresolution microscopy has enabled us to assemble a rather complete picture of lamin isoform supramolecular structure in mammalian somatic cell nuclei, light microscopy still lacks the resolution to allow determination of the fine structure of the meshworks. Early electron microscopic images of the nucleoplasmic-facing surface of *Xenopus* oocyte nuclei provided the best ultrastructural images of lamins in situ, revealing small regions of mesh-like structures of 10-nm filaments, with less-organized regions of interconnected filaments (Aebi *et al.*, 1986). However, oocytes express predominantly a single germ cell–specific B-type lamin, the structure of which may not reflect the structure of the multiple lamin isoforms expressed in somatic cells. Although 3D-SIM can realize subdiffraction resolution of ~110–130 nm, this is not sufficient to determine the ultrastructure of the lamin fibers in our images. For example, we do not know whether the lamin fibers we can resolve are composed of one or more lamin protofilaments or bundles of protofilaments. In addition, we cannot determine how the four meshworks are arranged in the lamina region due to limitations in *Z*-axis resolution. For example, individual isoform meshworks could each occupy a distinct layer, presumably with the farnesylated B-type lamins being more closely associated with the inner nuclear membrane and the A-type lamins more proximal to the peripheral chromatin. Alternatively, the four meshworks could be highly interwoven as in a cloth made up of four different threads.

The structures of the lamin meshworks may have important implications for the mechanical properties of the lamina (Funkhouser *et al.*, 2013; Koster *et al.*, 2015; Osmanagic-Myers *et al.*, 2015). Lamins A/C are believed to be responsible for the stiffness of the nucleus, and the loss of LA/C expression makes nuclei more susceptible to damage upon mechanical stress (Sullivan *et al.*, 1999; Lammerding *et al.*, 2006). On the other hand, changing the levels of B-type lamins has little or no effect

on the mechanical properties of the nucleus. The similarities in the structures of the lamin meshworks described in this study cannot explain these differences. Adding to the complexity of the mechanical properties of lamins, the meshworks are also linked to the cytoskeleton across the nuclear membranes by their association with LINC complexes (Meinke and Schirmer, 2015), to integral membrane proteins of the inner nuclear membrane (Brachner and Foisner, 2014), and to the chromatin underlying the NE (Guelen *et al.*, 2008; Zullo *et al.*, 2012). It will be of great interest to determine how altering lamin interactions with the cytoskeleton and chromatin affect, and in turn are affected by, the changing structure of the lamin meshworks. The methods we developed for the quantitative analysis of lamin meshworks will also enable us to begin to examine the role of posttranslational modifications to lamins, such as phosphorylation (Kochin *et al.*, 2014), and to the structural effect of the multitude of disease-causing lamin mutations (Shimi *et al.*, 2008).

To the best of our knowledge, this is the first comprehensive and quantitative superresolution study of the supramolecular structure of all lamin isoforms in the nuclear lamina of mammalian cells. This structural information is prerequisite to understanding not only normal lamin functions, but also their dysfunctions in the large number of human diseases caused by mutations in LMNA. These functions are wide ranging and include the regulation of chromatin organization and gene expression (Scaffidi and Misteli, 2006; Shumaker *et al.*, 2006; Taimen *et al.*, 2009), cell mechanics (Dahl *et al.*, 2006; Folker *et al.*, 2011; Ho *et al.*, 2013), senescence (McClintock *et al.*, 2006; Taimen *et al.*, 2009; Shimi *et al.*, 2011; Freund *et al.*, 2012), and DNA synthesis and damage repair (Liu *et al.*, 2005, 2011; Zhang *et al.*, 2011; Butin-Israeli *et al.*, 2013, 2015).

MATERIALS AND METHODS

DNA plasmids

The plasmid used for immortalizing cells, pBabe-puro largeTcDNA (plasmid #14088), and those used to express lamins for 3D-SIM (mEmerald-LaminA-C-18, plasmid #54138; and mEmerald-LaminB1-10, plasmid #54140) were obtained from Addgene (Cambridge, MA). The cDNA fragment encoding LB2 was amplified by PCR from pEGFP-LB2 (Moir *et al.*, 2000) and inserted into mEmerald-C1 (plasmid #53975; Addgene) using the InFusion HD cloning system (Clontech, Mountain View, CA). The cDNA fragment encoding LC was cut from pEGFP-myc-LC (Shimi *et al.*, 2008) and inserted into mEmerald-C1 cut with *Bsp*EI and *Bam*HI. All DNA constructs were verified by sequencing.

Cell culture and introduction of genes

Primary wt, *Lmna*$^{-/-}$, *Lmnb1*$^{-/-}$, and *Lmnb2*$^{-/-}$ MEFs were cultured in modified DMEM (Life Technologies, Carlsbad, CA) supplemented with 10% fetal calf serum, 50 U/ml penicillin G, 50 µg/ml streptomycin sulfate (Life Technologies), and 20 mM 4-(2-hydroxyethyl)-1-piperazineethanesulfonic acid (HEPES; Corning, Corning, NY) at 3% O_2 in a ProOx C21 incubator (Biospherix, Lacona, NY). MEFs were immortalized with SV40 large T antigen by retroviral transduction of the gene encoding the SV40 large T antigen as previously described (Shimi *et al.*, 2011). After selection with 2 µg/ml puromycin (Sigma-Aldrich, St. Louis, MO) for 3 d, immortalized MEFs were cultured in the growth medium without HEPES at 37°C in a humidified CO_2 incubator. Wild-type MEFs were transfected with mEmerald-LA, LB1, LB2, and LC using Lipofectamine 3000 (Life Technologies) in accordance with the product manuals. Transfection efficiencies were ~60%. Cells transiently expressing mEmerald-lamins were observed 48 h after transfection.

Indirect immunofluorescence

Cells were seeded on Gold Seal coverglasses (22 × 22 mm^2, no. 1.5; Thermo Fisher Scientific, Waltham, MA) for confocal microscopy and 3D-SIM. The cells were fixed with methanol for 10 min at −20°C. Lamins were stained with mouse monoclonal anti-LA (1:50; 133A2; Abcam, Cambridge, UK), rabbit polyclonal anti-LA (1:500; 323; Dechat *et al.*, 2007), goat polyclonal anti-LB1 (1:500; SC-6217; Santa Cruz Biotechnology, Dallas, TX), and rabbit monoclonal LB2 (1:100; EPR9701(B); Abcam), mouse monoclonal anti-LC (1:50; EM-11; Novus Biologicals, Littleton, CO), and rabbit polyclonal anti-LC (1:500; 321; Dechat *et al.*, 2007). The secondary antibodies used were donkey anti-mouse immunoglobulin G (IgG)–Alexa Fluor 488, donkey anti-mouse IgG–Alexa Fluor 568, donkey anti-rabbit IgG–Alexa Fluor 488, donkey anti-rabbit IgG–Alexa Fluor 568, donkey anti-goat IgG–Alexa Fluor 488, and donkey anti-goat IgG–Alexa Fluor 568 (all 1:500; Life Technologies). DNA was stained with Hoechst 33258 (Thermo Fisher Scientific). Processed coverslips were mounted on slides in 20 mM Tris-Cl (pH 9.0) with 50% glycerol and 1% *p*-phenylenediamine (Sigma-Aldrich) for confocal microscopy and ProLong Diamond antifade reagent (Life Technologies) for 3D-SIM.

Fluorescence microscopy

Confocal microscopy was carried with a Zeiss LSM 510 META microscope (Carl Zeiss, Jena, Germany) equipped with an oil immersion objective lens (PlanApochromat, 63×, 1.40 numerical aperture [NA]). 3D-SIM was carried out with a Nikon Structured Illumination Superresolution Microscope System (Nikon N-SIM; Nikon, Tokyo, Japan) using an oil immersion objective lens CFI SR (Apochromat TIRF 100×, 1.49 NA; Nikon). For 3D-SIM, 20 optical sections were taken at 50-nm intervals through the nuclear lamina region located at the face of the nucleus closest to the adherent surface of cells. For image reconstruction of 3D-SIM data, illumination modulation contrast, high-resolution noise suppression, and out-of-focus blur suppression were set with fixed values of 1, 0.75, and 0.15, respectively. For presentation, images were adjusted for brightness and contrast. Statistical values were determined using Student's *t* test. Color shifts in the *x*-, *y*-, and *z*-axes were corrected using MEFs into which TetraSpeck Fluorescent Microspheres (diameter 0.1 µm; Life Technologies) had been incorporated as described previously (Burnette *et al.*, 2011). Briefly, cells were incubated with TetraSpeck beads diluted 1:100 in phosphate-buffered saline (PBS) for 10 min at 37°C in a humidified CO_2 incubator. After a wash with PBS, these cells were fixed and processed for immunofluorescence with goat polyclonal anti-LB1 targeted with donkey anti-goat IgG–Alexa Fluor 488 and 568. Nikon Elements Advanced Research with an N-SIM module was used to reconstruct the structured illumination images.

Computing environment

Analysis was conducted on a Linux computing platform (BioHPC; UT Southwestern Medical Center, Dallas, TX). MATLAB (MathWorks, Natick, MA) was used as the base numerical computing package to analyze images and data. The Java library Bioformats was used to load images and metadata from the reconstructed Nikon ND2 files into MATLAB (Linkert *et al.*, 2010).

Initial meshwork segmentation

Meshwork segmentation was conducted by using an optimized steerable line filter based on linear combinations of Gaussian derivatives up to the fourth order (Jacob and Unser, 2004; Gaussian SD = 5 pixels = 158 nm based on empirical analysis of the images). Nonmaximal suppression (NMS; Canny, 1986) was applied to

identify the center of each filtered curvilinear structure, representing a meshwork edge. Only edges made of at least five pixels and within the nucleus mask (described later) were retained. After this, each pixel in the surviving edges was classified by the number of other pixels in its eight-connected neighborhood. Pixels with two connected neighbors were in the middle of an edge, pixels with more than two connected neighbors were junctions (i.e., intersections of two or more edges), and pixels with only one connected neighbor were endpoints.

To close gaps in the edges at junctions, manifesting themselves as premature endpoints, the orientation at each endpoint was determined by locating the centroid of the last six pixels from the endpoint and determining the direction of the vector from the centroid to the endpoint. Edges were extended from their original endpoint in that direction until a junction was created with other edges. The extensions were done by using the Bresenham line extension algorithm to create a series of 20 candidate pixels to add to each prior endpoint (Bresenham, 1965). Candidate pixels were added one at a time to all edges in parallel and were no longer added to an edge once its endpoint became a junction. The average extension length was three pixels. After extension, edges that did not end at a junction were deleted by removing spur pixels until none existed. The resulting connected meshwork was then skeletonized.

To simplify meshwork junctions to single pixels, short edges containing two pixels or less were reclassified as being part of a junction. The centroid of the connected junction pixels was determined and set as the junction location. At the same time, the original junction pixels were removed, creating temporary endpoints for the edges involved. These endpoints were then extended using the Bresenham line extension algorithm to the new junction location (Bresenham, 1965). This resulted in edges that started and ended at single-pixel junctions.

Edge auditing to produce final meshwork

Edges were audited in a multistep process in order to ensure that they matched well with the underlying lamin signal:

1. Any edges extending beyond the mask of the nucleus were removed, as the gap-closing procedure may have exceeded the mask.
2. Spurious edges without any associated enclosed faces were deleted.
3. For initial assessment of alignment of edges with the lamin signal and faces with areas devoid of lamin signal we calculated a metric for each face and its edges by 1) performing a Euclidean distance transform on the binary image with edge pixels marked as 1 and all other pixels marked as 0, 2) multiplying this distance by the intensity, and then 3) calculating the mean product per face. This was performed on the flattened image intensity (described in separate section later) to treat all faces similarly regardless of the global intensity variations. Smaller values of this metric indicate that the pixels in the middle of the face, farther away from the edge, have lower intensities, as they should. Edges were then individually deleted, and the metric for the new face (created by combining the two faces on either side of the edge) was calculated. If it was smaller than the minimum value of the metric for the two former faces, the edge was permanently removed, as this meant the new face had a better quality than either of the former faces.
4. Edges were audited based on their mean intensity to eliminate dim edges that are most likely false positives. Specifically, a fluorescence intensity threshold was determined as the value at which the difference between the cumulative distribution functions of the intensities located within the nucleus mask and outside the mask was maximal. Edges were then required to have a mean intensity of at least half this threshold.
5. Edges were audited based on the variation of intensity along their length to distinguish between true positive edges, expected to have a relatively uniform intensity, and false positive edges, expected to have highly fluctuating intensities. For this, the normalized intensity range of an edge was calculated as the difference between its maximum and minimum intensities divided by its mean intensity. A unimodal threshold of this normalized range for all edges was calculated by the Rosin algorithm (Rosin, 2001), and edges with a normalized range below this threshold were retained.
6. We sought to classify pixels as low or high intensity with respect to their local area. For this, two thresholds were used to classify pixels within the nucleus based on the flattened image intensity. 1) A threshold (T_{Otsu}) based on Otsu's method (Otsu, 1979) was determined from the intensity distribution across the whole image. 2) A second, lower threshold (T_{mask}) was generated as in step 4 based on comparing the intensity distributions inside versus outside the nucleus. We then used these thresholds to apply a criterion that each edge should contain at least the same proportion of high-intensity pixels as the proportion of high-intensity pixels in the nucleus. The proportion of high-intensity pixels in the lamina ($P_{nucleus}$) was defined as the fraction of pixels within the nucleus mask with intensity greater than T_{Otsu}, as T_{Otsu} was derived without prior information about the nucleus mask. The proportion of each edge greater than T_{mask} (P_{edge}) was then evaluated for comparison since edges are necessarily contained within the nucleus. Edges with $P_{edge} < P_{nucleus}$ were then deleted.
7. For final assessment of alignment of edges with the lamin signal and faces with areas devoid of lamin signal, step 3 was repeated, as the removal of edges by steps 4–6 might generate a new landscape of faces, allowing for more edges to be removed improving quality further. In this final evaluation, an edge was removed if its deletion resulted in a face with a metric smaller than or equal to the minimum value of the metric for the two former faces, thus avoiding oversegmentation of the meshwork.

Cell nucleus mask

A mask for the cell nucleus was created by using hysteresis thresholding between the 90th and 75th percentiles of the nonzero pixels in the NMS. Morphological closing by a disk with a radius of 10 pixels, filling, and opening with a disk with a radius of 50 pixels were used to create a binary image without holes. The largest connected component of the image covering <70% of the image was selected as the mask for the nucleus. Nuclei consuming >70% of the image were excluded from meshwork segmentation and analysis since there would be insufficient background pixels to determine thresholds for auditing.

Image intensity flattening

To evaluate how well edges contrasted with their local neighborhood while being adaptive to global differences in intensity, long-range background variations were removed. This allowed us to minimize false-positive segmentation of out-of-focus fluorescence. Specifically, images were filtered with a Gaussian of SD = 10 pixels, and then the images were divided by the response to create a flattened image.

Meshwork property characterization and comparison

Meshwork properties were calculated by evaluating the properties of the component edges, junctions, and faces. Many properties, such as edge length, face area, and face eccentricity, were available by encoding these structures as connected components and using the built-in MATLAB command regionprops. For example, eccentricity is a measure of shape that is 0 for a circle or 1 for a line segment. The number of edges per face was calculated to ensure that the counted edges actually enclose each face as follows:

1. Dilate the face by a square structure element with a width of five pixels.
2. Identify candidate edges that overlay the dilated face.
3. Identify the junctions associated with each candidate edge.
4. Count the number of candidate edges that meet at each junction.
5. Eliminate from candidacy the edges where they are the only edge associated with a junction.
6. Eliminate from candidacy the edges whose midpoints do not overlay the dilated face.
7. Accept the remaining edge candidates.

Properties were aggregated for multiple cells in the same condition to create sample distributions, which were then compared. When comparing distributions of properties of lamin meshworks in wild-type cells, the compared distributions originated from the same set of cells. When comparing distributions between wild-type cells and mutants, distributions derived from the same label were compared.

The q-q plots were used to visually depict these comparisons using the built-in q-q plot MATLAB function at the specified percentiles. The plots were further annotated to more clearly indicate the median of each distribution. In addition, a least-squares linear regression was performed to determine the slope of the line that best fit the 25th through 75th percentiles, which was then used to annotate the graph. Generally, a slope of 1 indicates equal distributions. Slopes differing from 1 indicate that the distribution on the *x*-axis could be scaled by this slope to match the distribution on the *y*-axis.

ACKNOWLEDGMENTS

We thank Josh Rappoport and Constadina Arvanitis in the Nikon Imaging Center at Northwestern University and Lynne Chang of Nikon Instruments for assistance with 3D-SIM. This work was supported by National Institutes of Health Grant GM106023 (R.D.G. and Y.Z.), a grant from the Progeria Research Foundation (R.D.G.), and Cancer Prevention and Research Institute of Texas Recruitment Award R1216 and the UT Southwestern Endowed Scholars Program (K.J.).

REFERENCES

Aebi U, Cohn J, Buhle L, Gerace L (1986). The nuclear lamina is a meshwork of intermediate-type filaments. Nature 323, 560–564.

Ben-Harush K, Wiesel N, Frenkiel-Krispin D, Moeller D, Soreq E, Aebi U, Herrmann H, Gruenbaum Y, Medalia O (2009). The supramolecular organization of the C. elegans nuclear lamin filament. J Mol Biol 386, 1392–1402.

Biamonti G, Giacca M, Perini G, Contreas G, Zentilin L, Weighardt F, Guerra M, Della Valle G, Saccone S, Riva S, *et al.* (1992). The gene for a novel human lamin maps at a highly transcribed locus of chromosome 19 which replicates at the onset of S-phase. Mol Cell Biol 12, 3499–3506.

Brachner A, Foisner R (2014). Lamina-associated polypeptide (LAP)2alpha and other LEM proteins in cancer biology. Adv Exp Med Biol 773, 143–163.

Bresenham JE (1965). Algorithm for computer control of a digital plotter. IBM Syst J 4, 25–30.

Burnette DT, Sengupta P, Dai Y, Lippincott-Schwartz J, Kachar B (2011). Bleaching/blinking assisted localization microscopy for superresolution imaging using standard fluorescent molecules. Proc Natl Acad Sci USA 108, 21081–21086.

Butin-Israeli V, Adam SA, Goldman RD (2013). Regulation of nucleotide excision repair by nuclear lamin b1. PLoS One 8, e69169.

Butin-Israeli V, Adam SA, Jain N, Otte GL, Neems D, Wiesmuller L, Berger SL, Goldman RD (2015). Role of lamin b1 in chromatin instability. Mol Cell Biol 35, 884–898.

Canny J (1986). A computational approach to edge detection. IEEE Trans Pattern Anal Mach Intell 8, 679–698.

Constantinescu D, Gray HL, Sammak PJ, Schatten GP, Csoka AB (2006). Lamin A/C expression is a marker of mouse and human embryonic stem cell differentiation. Stem Cells 24, 177–185.

Dahl KN, Scaffidi P, Islam MF, Yodh AG, Wilson KL, Misteli T (2006). Distinct structural and mechanical properties of the nuclear lamina in Hutchinson-Gilford progeria syndrome. Proc Natl Acad Sci USA 103, 10271–10276.

Dechat T, Shimi T, Adam SA, Rusinol AE, Andres DA, Spielmann HP, Sinensky MS, Goldman RD (2007). Alterations in mitosis and cell cycle progression caused by a mutant lamin A known to accelerate human aging. Proc Natl Acad Sci USA 104, 4955–4960.

Eckersley-Maslin MA, Bergmann JH, Lazar Z, Spector DL (2013). Lamin A/C is expressed in pluripotent mouse embryonic stem cells. Nucleus 4, 53–60.

Fawcett DW (1966). On the occurrence of a fibrous lamina on the inner aspect of the nuclear envelope in certain cells of vertebrates. Am J Anat 119, 129–145.

Fisher DZ, Chaudhary N, Blobel G (1986). cDNA sequencing of nuclear lamins A and C reveals primary and secondary structural homology to intermediate filament proteins. Proc Natl Acad Sci USA 83, 6450–6454.

Folker ES, Ostlund C, Luxton GW, Worman HJ, Gundersen GG (2011). Lamin A variants that cause striated muscle disease are defective in anchoring transmembrane actin-associated nuclear lines for nuclear movement. Proc Natl Acad Sci USA 108, 131–136.

Freeman W, Adelson E (1991). The design and use of steerable filters. IEEE Trans Pattern Anal Mach Intell 13, 891–906.

Freund A, Laberge RM, Demaria M, Campisi J (2012). Lamin B1 loss is a senescence-associated biomarker. Mol Biol Cell 23, 2066–2075.

Funkhouser CM, Sknepnek R, Shimi T, Goldman AE, Goldman RD, Olvera de la Cruz M (2013). Mechanical model of blebbing in nuclear lamin meshworks. Proc Natl Acad Sci USA 110, 3248–3253.

Gerace L, Blobel G (1980). The nuclear envelope lamina is reversibly depolymerized during mitosis. Cell 19, 277–287.

Gerace L, Blum A, Blobel G (1978). Immunocytochemical localization of the major polypeptides of the nuclear pore complex-lamina fraction. Interphase and mitotic distribution. J Cell Biol 79, 546–566.

Goldberg MW, Huttenlauch I, Hutchison CJ, Stick R (2008). Filaments made from A- and B-type lamins differ in structure and organization. J Cell Sci 121, 215–225.

Goldman AE, Maul G, Steinert PM, Yang HY, Goldman RD (1986). Keratin-like proteins that coisolate with intermediate filaments of BHK-21 cells are nuclear lamins. Proc Natl Acad Sci USA 83, 3839–3843.

Grossman E, Dahan I, Stick R, Goldberg MW, Gruenbaum Y, Medalia O (2012). Filaments assembly of ectopically expressed Caenorhabditis elegans lamin within Xenopus oocytes. J Struct Biol 177, 113–118.

Guelen L, Pagie L, Brasset E, Meuleman W, Faza MB, Talhout W, Eussen BH, de Klein A, Wessels L, de Laat W, van Steensel B (2008). Domain organization of human chromosomes revealed by mapping of nuclear lamina interactions. Nature 453, 948–951.

Guo M, Ehrlicher AJ, Mahammad S, Fabich H, Jensen MH, Moore JR, Fredberg JJ, Goldman RD, Weitz DA (2013). The role of vimentin intermediate filaments in cortical and cytoplasmic mechanics. Biophys J 105, 1562–1568.

Guo Y, Kim Y, Shimi T, Goldman RD, Zheng Y (2014). Concentration-dependent lamin assembly and its roles in the localization of other nuclear proteins. Mol Biol Cell 25, 1287–1297.

Haraguchi T, Kojidani T, Koujin T, Shimi T, Osakada H, Mori C, Yamamoto A, Hiraoka Y (2008). Live cell imaging and electron microscopy reveal dynamic processes of BAF-directed nuclear envelope assembly. J Cell Sci 121, 2540–2554.

Harr JC, Luperchio TR, Wong X, Cohen E, Wheelan SJ, Reddy KL (2015). Directed targeting of chromatin to the nuclear lamina is mediated by chromatin state and A-type lamins. J Cell Biol 208, 33–52.
Heitlinger E, Peter M, Haner M, Lustig A, Aebi U, Nigg EA (1991). Expression of chicken lamin B2 in Escherichia coli: characterization of its structure, assembly, and molecular interactions. J Cell Biol 113, 485–495.
Ho CY, Jaalouk DE, Vartiainen MK, Lammerding J (2013). Lamin A/C and emerin regulate MKL1-SRF activity by modulating actin dynamics. Nature 497, 507–511.
Hoger TH, Zatloukal K, Waizenegger I, Krohne G (1990). Characterization of a second highly conserved B-type lamin present in cells previously thought to contain only a single B-type lamin. Chromosoma 99, 379–390.
Jacob M, Unser M (2004). Design of steerable filters for feature detection using canny-like criteria. IEEE Trans Pattern Anal Mach Intell 26, 1007–1019.
Kim Y, Sharov AA, McDole K, Cheng M, Hao H, Fan CM, Gaiano N, Ko MS, Zheng Y (2011). Mouse B-type lamins are required for proper organogenesis but not by embryonic stem cells. Science 334, 1706–1710.
Kim Y, Zheng X, Zheng Y (2013). Proliferation and differentiation of mouse embryonic stem cells lacking all lamins. Cell Res 23, 1420–1423.
Kochin V, Shimi T, Torvaldson E, Adam SA, Goldman A, Pack CG, Melo-Cardenas J, Imanishi SY, Goldman RD, Eriksson JE (2014). Interphase phosphorylation of lamin A. J Cell Sci 127, 2683–2696.
Kolb T, Maass K, Hergt M, Aebi U, Herrmann H (2011). Lamin A and lamin C form homodimers and coexist in higher complex forms both in the nucleoplasmic fraction and in the lamina of cultured human cells. Nucleus 2, 425–433.
Koster S, Weitz DA, Goldman RD, Aebi U, Herrmann H (2015). Intermediate filament mechanics in vitro and in the cell: from coiled coils to filaments, fibers and networks. Curr Opin Cell Biol 32, 82–91.
Lammerding J, Fong LG, Ji JY, Reue K, Stewart CL, Young SG, Lee RT (2006). Lamins A and C but not lamin B1 regulate nuclear mechanics. J Biol Chem 281, 25768–25780.
Linkert M, Rueden CT, Allan C, Burel J-M, Moore W, Patterson A, Loranger B, Moore J, Neves C, Macdonald D, *et al.* (2010). Metadata matters: access to image data in the real world. J. Cell Biol. 189, 777–782.
Lin F, Worman HJ (1993). Structural organization of the human gene encoding nuclear lamin A and nuclear lamin C. J Biol Chem 268, 16321–16326.
Lin F, Worman HJ (1995). Structural organization of the human gene (LMNB1) encoding nuclear lamin B1. Genomics 27, 230–236.
Liu GH, Barkho BZ, Ruiz S, Diep D, Qu J, Yang SL, Panopoulos AD, Suzuki K, Kurian L, Walsh C, *et al.* (2011). Recapitulation of premature ageing with iPSCs from Hutchinson-Gilford progeria syndrome. Nature 472, 221–225.
Liu B, Wang J, Chan KM, Tjia WM, Deng W, Guan X, Huang JD, Li KM, Chau PY, Chen DJ, *et al.* (2005). Genomic instability in laminopathy-based premature aging. Nat Med 11, 780–785.
Lund EG, Duband-Goulet I, Oldenburg A, Buendia B, Collas P (2015). Distinct features of lamin A-interacting chromatin domains mapped by ChIP-sequencing from sonicated or micrococcal nuclease-digested chromatin. Nucleus 6, 30–39.
Lund E, Oldenburg AR, Collas P (2014). Enriched domain detector: a program for detection of wide genomic enrichment domains robust against local variations. Nucleic Acids Res 42, e92.
Maeno H, Sugimoto K, Nakajima N (1995). Genomic structure of the mouse gene (Lmnb1) encoding nuclear lamin B1. Genomics 30, 342–346.
Maeshima K, Yahata K, Sasaki Y, Nakatomi R, Tachibana T, Hashikawa T, Imamoto F, Imamoto N (2006). Cell-cycle-dependent dynamics of nuclear pores: pore-free islands and lamins. J Cell Sci 119, 4442–4451.
McClintock D, Gordon LB, Djabali K (2006). Hutchinson-Gilford progeria mutant lamin A primarily targets human vascular cells as detected by an anti-Lamin A G608G antibody. Proc Natl Acad Sci USA 103, 2154–2159.
McKeon FD, Kirschner MW, Caput D (1986). Homologies in both primary and secondary structure between nuclear envelope and intermediate filament proteins. Nature 319, 463–468.
Meinke P, Schirmer EC (2015). LINC'ing form and function at the nuclear envelope. FEBS Lett 589, 2514–2521.
Meuleman W, Peric-Hupkes D, Kind J, Beaudry JB, Pagie L, Kellis M, Reinders M, Wessels L, van Steensel B (2013). Constitutive nuclear lamina-genome interactions are highly conserved and associated with A/T-rich sequence. Genome Res 23, 270–280.
Moir RD, Yoon M, Khuon S, Goldman RD (2000). Nuclear lamins A and B1: different pathways of assembly during nuclear envelope formation in living cells. J Cell Biol 151, 1155–1168.
Muchir A, Medioni J, Laluc M, Massart C, Arimura T, van der Kooi AJ, Desguerre I, Mayer M, Ferrer X, Briault S, *et al.* (2004). Nuclear envelope alterations in fibroblasts from patients with muscular dystrophy, cardiomyopathy, and partial lipodystrophy carrying lamin A/C gene mutations. Muscle Nerve 30, 444–450.
Novelli G, Muchir A, Sangiuolo F, Helbling-Leclerc A, D'Apice MR, Massart C, Capon F, Sbraccia P, Federici M, Lauro R, *et al.* (2002). Mandibuloacral dysplasia is caused by a mutation in LMNA-encoding lamin A/C. Am J Hum Genet 71, 426–431.
Osmanagic-Myers S, Dechat T, Foisner R (2015). Lamins at the crossroads of mechanosignaling. Genes Dev 29, 225–237.
Otsu N (1979). A threshold selection method from gray-level histograms. IEEE Trans Syst Man Cybernet 9, 62–66.
Parry DA, Conway JF, Steinert PM (1986). Structural studies on lamin. Similarities and differences between lamin and intermediate-filament proteins. Biochem J 238, 305–308.
Rober RA, Weber K, Osborn M (1989). Differential timing of nuclear lamin A/C expression in the various organs of the mouse embryo and the young animal: a developmental study. Development 105, 365–378.
Rosin PL (2001). Unimodal thresholding. Pattern Recogn 34, 2083–2096.
Scaffidi P, Misteli T (2006). Lamin A-dependent nuclear defects in human aging. Science 312, 1059–1063.
Schermelleh L, Carlton PM, Haase S, Shao L, Winoto L, Kner P, Burke B, Cardoso MC, Agard DA, Gustafsson MG, *et al.* (2008). Subdiffraction multicolor imaging of the nuclear periphery with 3D structured illumination microscopy. Science 320, 1332–1336.
Shimi T, Butin-Israeli V, Adam SA, Hamanaka RB, Goldman AE, Lucas CA, Shumaker DK, Kosak ST, Chandel NS, Goldman RD (2011). The role of nuclear lamin B1 in cell proliferation and senescence. Genes Dev 25, 2579–2593.
Shimi T, Pfleghaar K, Kojima S, Pack CG, Solovei I, Goldman AE, Adam SA, Shumaker DK, Kinjo M, Cremer T, Goldman RD (2008). The A- and B-type nuclear lamin networks: microdomains involved in chromatin organization and transcription. Genes Dev 22, 3409–3421.
Shumaker DK, Dechat T, Kohlmaier A, Adam SA, Bozovsky MR, Erdos MR, Eriksson M, Goldman AE, Khuon S, Collins FS, *et al.* (2006). Mutant nuclear lamin A leads to progressive alterations of epigenetic control in premature aging. Proc Natl Acad Sci USA 103, 8703–8708.
Stewart C, Burke B (1987). Teratocarcinoma stem cells and early mouse embryos contain only a single major lamin polypeptide closely resembling lamin B. Cell 51, 383–392.
Stuurman N, Sasse B, Fisher PA (1996). Intermediate filament protein polymerization: molecular analysis of Drosophila nuclear lamin head-to-tail binding. J Struct Biol 117, 1–15.
Sullivan T, Escalante-Alcalde D, Bhatt H, Anver M, Bhat N, Nagashima K, Stewart CL, Burke B (1999). Loss of A-type lamin expression compromises nuclear envelope integrity leading to muscular dystrophy. J Cell Biol 147, 913–920.
Taimen P, Pfleghaar K, Shimi T, Moller D, Ben-Harush K, Erdos MR, Adam SA, Herrmann H, Medalia O, Collins FS, *et al.* (2009). A progeria mutation reveals functions for lamin A in nuclear assembly, architecture, and chromosome organization. Proc Natl Acad Sci USA 106, 20788–20793.
Vergnes L, Peterfy M, Bergo MO, Young SG, Reue K (2004). Lamin B1 is required for mouse development and nuclear integrity. Proc Natl Acad Sci USA 101, 10428–10433.
Vigouroux C, Auclair M, Dubosclard E, Pouchelet M, Capeau J, Courvalin JC, Buendia B (2001). Nuclear envelope disorganization in fibroblasts from lipodystrophic patients with heterozygous R482Q/W mutations in the lamin A/C gene. J Cell Sci 114, 4459–4468.
Zhang C, Jenkins H, Goldberg MW, Allen TD, Hutchison CJ (1996). Nuclear lamina and nuclear matrix organization in sperm pronuclei assembled in Xenopus egg extract. J Cell Sci 109, 2275–2286.
Zhang J, Lian Q, Zhu G, Zhou F, Sui L, Tan C, Mutalif RA, Navasankari R, Zhang Y, Tse HF, *et al.* (2011). A human iPSC model of Hutchinson Gilford Progeria reveals vascular smooth muscle and mesenchymal stem cell defects. Cell Stem Cell 8, 31–45.
Zheng X, Kim Y, Zheng Y (2015). Identification of lamin B-regulated chromatin regions based on chromatin landscapes. Mol Biol Cell 26, 2685–2697.
Zullo JM, Demarco IA, Pique-Regi R, Gaffney DJ, Epstein CB, Spooner CJ, Luperchio TR, Bernstein BE, Pritchard JK, Reddy KL, Singh H (2012). DNA sequence-dependent compartmentalization and silencing of chromatin at the nuclear lamina. Cell 149, 1474–1487.